

Deblurring for Spiral Real-Time MRI Using Convolutional Neural Networks

Yongwan Lim*, MS, Shrikanth Narayanan, PhD, Krishna S. Nayak, PhD

*Ming Hsieh Department of Electrical and Computer Engineering, Viterbi School of
Engineering, University of Southern California, Los Angeles, California, USA*

* Corresponding author:

Yongwan Lim, MS

3740 McClintock Ave, EEB 400

University of Southern California, Los Angeles, CA, 90089-2564

Phone: (213) 479-5015 / Fax: (213) 740-4651

E-mail: yongwanl@usc.edu

Journal: Magnetic Resonance in Medicine

Category: Full Paper

Number of words: 4964/ 5000

Number of figures and tables: 10 / 10

Running head: Deblurring for spiral RT-MRI using CNNs

ABSTRACT

Purpose: To develop and evaluate a fast and effective method for deblurring spiral real-time magnetic resonance imaging (**RT-MRI**) using convolutional neural networks (**CNN**).

Methods: We demonstrate a 3-layer residual CNN to correct image domain off-resonance artifacts in speech production spiral RT-MRI without knowledge of field maps. The architecture is motivated by the multi-frequency segmentation method. Spatially varying off-resonance blur is synthetically generated by using discrete object approximation and field maps with data augmentation from a large database of 2D human speech production RT-MRI. The impact of off-resonance frequency range, appearance of blurring, and readout durations is validated with synthetic data. The proposed method is tested using synthetic test and in vivo data with longer readouts, quantitatively using image quality metrics and qualitatively via visual inspection, and via comparison with conventional deblurring methods.

Results: Deblurring performance was found superior to a current auto-calibrated method for in vivo data, and only slightly worse than ideal reconstruction with perfect knowledge of the field map for synthetic test data. CNN deblurring made it possible to visualize articulator boundaries with readouts up to 8 ms at 1.5 T, which is 3-fold longer than the current standard practice. The computation time was 12.3 ± 2.2 ms per-frame, enabling a low-latency processing for RT-MRI applications.

Conclusion: CNN-deblurring is a practical, efficient, and field-map-free approach for deblurring of spiral RT-MRI. In the context of speech production imaging this can enable 1.7-fold improvement in scan efficiency and the use of spiral readouts at higher field strengths such as 3 T.

Keywords: artifact correction, convolutional neural networks, deblurring, off-resonance, real-time MRI, speech production

INTRODUCTION

Spiral data sampling is used in a variety of MRI applications due to its favorable properties such as efficient k-space coverage and low sensitivity to motion and flow (1,2). It requires only as little as one or a few TRs to achieve Nyquist sampling of k-space, and provides excellent velocity point spread function (**PSF**), and reduces motion artifacts due to its natural oversampling at the k-space center (3,4). Spiral sampling is well-suited for advanced reconstruction algorithms such as compressed sensing when combined with strategies such as under sampling and golden angle scheme (5,6). Spiral imaging is also widely used for real-time MRI (**RT-MRI**) where the capability of capturing rapid motion is crucial such as in cardiac imaging and speech production imaging (6–12).

One major limitation of spiral sampling is image blurring due to off-resonance (13). Off-resonance causes the accumulation of phase error along the readout in k-space domain, resulting in blurring and/or signal loss in image domain. To date, this artifact remains the dominant challenge for several RT-MRI applications: In speech RT-MRI it degrades image quality most significantly at air-tissue boundaries which include the vocal tract articulators of interest (14–16). In cardiac RT-MRI, it degrades image quality in the lateral wall and adjacent to draining veins, and around implanted metal (e.g. valve clips, etc) (10,17). In interventional RT-MRI, it may degrade image quality around the tools used to perform intervention (depending on the precise composition of the tools) (18). These artifacts are most pronounced with long readout durations which is precisely when spiral provides the greatest efficiency. In speech production RT-MRI, the convention is to use extremely short readouts (≤ 2.5 ms at 1.5 T) (16).

Many spiral off-resonance correction methods have been proposed in the literature. Most existing methods require prior information about the spatial distribution of the off-resonance, also called the *field map*, $\Delta f(x,y)$ (19–25). For RT-MRI, this field map needs to be updated frequently throughout the acquisition window because local off-resonance changes as motion occurs. Several research groups have proposed to estimate *dynamic* field maps either from interleaved two TE acquisition using conventional phase difference method (14) or from single-TE acquisition after coil phase compensation (15). Common limitations of these approaches are field map estimation errors due to off-resonance induced image distortion and/or reduced scan efficiency which is undesirable for RT-MRI.

Given a field map, the conventional approach to deblur the image is conjugate phase reconstruction (**CPR**) (19,20) or one of its several variants (21,22,26). One such variant is frequency-segmentation which reconstructs basis images at demodulation frequencies and applies spatially-varying masks to the basis images to form a desired sharp image. While it is an efficient approximation to assume off-resonance to be spatially smoothly varying, the assumptions are typically violated at air-tissue interfaces. Alternatively, iterative approaches (27,28) are known to be effective at resolving spatially abruptly varying off-resonance at the cost of increased computation complexity. Note that, neither iterative nor non-iterative approaches are able to overcome the performance dependence on the quality of the estimated field maps.

Recently, convolutional neural networks (**CNN**) have shown promise in solving this deblurring task. Zeng et al. (29) have proposed a 3D residual CNN architecture to correct off-resonance artifacts from long-readout 3D cones scan. Specifically, off-resonance was framed as a spatially varying deconvolution problem. Synthetic data were generated by simulating zeroth-order global off-resonance at a certain range of demodulation frequency. The trained network was applied successfully to long-readout pediatric body MRA scans. The underlying principle that explains why and how CNNs work well in this deblurring task would be owing to the combinatorial nature of nonlinearities such as rectified linear unit (**ReLU**) in CNN models. Traditional methods require field maps (19–25) or focus metrics (30–32) to estimate the spatially-varying mask. In contrast, CNNs utilize prior information about characteristics of off-resonance in the synthesized training data, while ReLU nonlinearities provide the mask to the convolution filters, which enables spatially-varying convolution (33). Once the network is trained, the feedforward operation of CNNs generates a desired sharp image given a blurry image input in an end-to-end manner, without explicit knowledge of field maps.

In this work, we utilize a simple 3-layer CNN architecture to learn the mapping between distorted and distortion-free images for 2D spiral RT-MRI of human speech production. We consider this application (16,34,35) because off-resonance appears as spatially (and temporally) abruptly varying blur, degrades image quality at the vocal tract articulators of interest, and therefore is a fundamental limitation to address. We leverage field maps estimated from a previously proposed dynamic off-resonance correction method (15). Specifically, we synthesize spatially varying off-resonance by using the

estimated field maps with various augmentation strategies. We test the impact of various data augmentation strategies on deblurring performance and generalization in terms of several image quality metrics. We evaluate the proposed method using synthesized and real test data set and compare its performance quantitatively using metrics and qualitatively via visual inspection against conventional deblurring methods.

THEORY

Image distortion due to off-resonance

In spiral MRI, off-resonance results in a spatially varying blur that can be characterized by a PSF (30). Off-resonance causes the local phase accumulation in the k-space signal. In spatial domain, this can be viewed as an object being convolved with spatially varying filter kernel (PSF) that is determined by the local off-resonance and trajectory-specific parameters such as a readout time map. Here, we briefly introduce this representation in the discrete domain, which we use throughout this paper.

In the presence of off-resonance effects, the signal equation after discretization approximation (27,28) can be expressed as:

$$y_i \approx \sum_{j=1}^{N_p} x_j e^{-i2\pi f_j t_i} e^{-i2\pi(\mathbf{k}_i \cdot \mathbf{r}_j)} \quad [1]$$

where \mathbf{k}_i and \mathbf{r}_j represent k-space and spatial coordinates for $i = 1, \dots, N_d$ and $j = 1, \dots, N_p$, respectively; y_i is the complex k-space measurement at time $t_i \in [T_E, T_E + T_{read}]$ defining $t_1 = T_E$ as the start of the readout; T_{read} is the readout duration and T_E is echo time. x_j is the transverse magnetization of an object at location \mathbf{r}_j . f_j is off-resonance frequency present at location \mathbf{r}_j . Here $e^{-i2\pi f_j t_i}$ is the local phase error that is induced by off-resonance present at location \mathbf{r}_j and is multiplied to the k-space signal at \mathbf{k}_i . Note that Equation [1] can be expressed in matrix-vector form as $\mathbf{y} = \mathbf{A}_f \mathbf{x}$ where $\mathbf{y} = (y_1, \dots, y_{N_d}) \in \mathbb{C}^{N_d}$, $\mathbf{x} = (x_1, \dots, x_{N_p}) \in \mathbb{C}^{N_p}$, $\mathbf{f} = (f_1, \dots, f_{N_p}) \in \mathbb{R}^{N_p}$, and $\mathbf{A}_f \in \mathbb{C}^{N_d \times N_p}$ with $[\mathbf{A}_f]_{ij} = e^{-i2\pi f_j t_i} e^{-i2\pi(\mathbf{k}_i \cdot \mathbf{r}_j)}$. In the absence of off-resonance effects (i.e., $\mathbf{f} = \mathbf{0}$), \mathbf{A}_f is reduced to the conventional (non-uniform) Fourier basis matrix \mathbf{A}_0 with $[\mathbf{A}_0]_{ij} = e^{-i2\pi(\mathbf{k}_i \cdot \mathbf{r}_j)}$.

Without considering off-resonance effect, we could reconstruct a blurry image

$\tilde{\mathbf{x}} \in \mathbb{C}^{N_p}$ by applying $\mathbf{A}_0^T \mathbf{W}$ to \mathbf{y} as follows:

$$\tilde{\mathbf{x}} = \mathbf{A}_0^T \mathbf{W} \mathbf{y} = \mathbf{A}_0^T \mathbf{W} \mathbf{A}_f \mathbf{x} = \mathbf{H}_f \mathbf{x} \quad [2]$$

where T denotes the conjugate transpose of a matrix. $\mathbf{W} \in \mathbb{R}^{N_d \times N_d}$ is a diagonal matrix whose diagonal is given by $\mathbf{w} = (w_1, \dots, w_{N_d})$; \mathbf{w} denotes a weight to compensate for a non-uniform k -space sampling density. Here, $\mathbf{H}_f \in \mathbb{C}^{N_p \times N_p}$ is a blurring operator matrix defining $[\mathbf{H}_f]_{j,k} = \sum_{i=1}^{N_d} w_i e^{-i2\pi f_k t_i} e^{i2\pi \mathbf{k}_i \cdot (\mathbf{r}_j - \mathbf{r}_k)}$. The k -th column of \mathbf{H}_f corresponds to the discretized PSF for a point-source located at \mathbf{r}_k . The effect of off-resonance can be seen as a spatially varying convolution since the PSF is shift-variant due to $e^{-i2\pi f_k t_i}$ with non-zero f_k . Whether the PSF is sharp or blurred is dependent on the off-resonance frequency (f_k) given the trajectory-specific parameters – trajectory \mathbf{k}_i and time map t_i for $i = 1, \dots, N_d$. Likewise, the readout time ($T_{read} = t_{N_d}$) determines the shape of the PSF given f_k . For example, the larger f_k and/or the longer T_{read} are, the more phase error of $e^{-i2\pi f_k t_i}$ is accrued, therefore increasing the spread of the PSF.

Approximation of spatially varying blur

The blurring operator \mathbf{H}_f can be considered a low-rank matrix based on the fact that many spatial locations will share the same off-resonance frequency. This assumption allows decompositions of the shift-variant blurring operator \mathbf{H}_f as a sum of L ($L \ll N_p$; N_p = the number of pixels) convolutions (i.e., shift-invariant blurring operators) with prior weightings (36):

$$\mathbf{H}_f \approx \sum_{l=1}^L \mathbf{H}_l \mathbf{S}_l \quad [3]$$

where \mathbf{H}_l denotes the convolution matrix, whose columns are shifted versions of an appropriate PSF and \mathbf{S}_l is a diagonal matrix whose diagonal is determined by the off-resonance f . For example, in frequency-segmentation (26), \mathbf{H}_l can be given by PSFs at a set of equally spaced L off-resonance frequencies and \mathbf{S}_l is a spatially varying mask that has a diagonal element of 1 if a corresponding pixel needs to be assigned to the l -th frequency or 0 otherwise. Including time-segmentation and singular value decomposition,

there are other approaches possible for the matrix decomposition (28,36).

The off-resonance $f(x,y)$ is often assumed to have smooth spatial variation (19,20,21,22,26), which mathematically translates into assuming that the columns of the blurring matrix H_f are orthogonal (25). This assumption is often reasonable because B0 inhomogeneity and susceptibility cause smooth variations in space (37). Under this assumption, the deblurred image could be obtained from Equation [2] and [3] by

$$\hat{x} = H_f^T \tilde{x} = \sum_{l=1}^L S_l H_l^T \tilde{x} \quad [4]$$

This can be interpreted as a blurred image \tilde{x} being convolved with H_l^T , followed by spatially varying weighted (or masking) (S_l) summation.

Spatially varying deblurring using CNN

Interestingly, the solution described in Equation [4] would resemble the feedforward operation of a simple two-layer CNN. Let us say a two-layer CNN consisting of a convolution operator ξ_l^1 and ReLU nonlinear activation $\sigma(\cdot)$ in the first layer and a 1×1 convolution ξ_l^2 with no activation in the second layer. Then the feedforward operation is given as follows:

$$\hat{x} = \sum_{l=1}^L \xi_l^2 \sigma(\xi_l^1 \tilde{x}) \quad [5]$$

It would be possible that spatially varying weighting (S_l) followed by the summation in Equation [4] could be achieved by ReLU nonlinear operation followed by a 1×1 convolution in the second layer in the two-layer CNN. The main difference between Equations [4] and [5] is that the spatially-varying mask S_l would be determined by field maps f , whereas in CNN the combination of ReLU $\sigma(\cdot)$ and the succeeding convolution ξ_l^2 enables spatially-varying convolution. Rather than relying on measuring exam-specific field maps, the CNN would learn from training samples to recognize and undo characteristic effects of off-resonance.

METHODS

Network Architecture

Figure 1A illustrates the proposed network architecture, inspired by the derivation provided in the previous section. The input is distorted images, and the output is distortion-corrected images. The network is composed of 3 convolutional layers. The first 2 layers apply 2D convolutions, followed by ReLU operation. The last layer applies 2D convolution with 1×1 spatial support. We implement the convolution shown in Equation [4] using the first two cascaded convolution filters to increase the number of representation. The combination of ReLU in the second layer and 1×1 convolution in the third layer would be analogous to spatially-varying weighting and summation shown in Equation [4]. We experimentally found that adding a skip connection improves deblurring performance (comparison not shown). Both input and output of the networks consist of two channels (real and imaginary). The number of filter width is set to $n_1 = 64, n_2 = 32, n_3 = 2$. We choose $f_1 = 9, f_2 = 5$, and $f_3 = 1$. We experimentally determined convolutional filter sizes of f_1 and f_2 that give the best deblurring performance in terms of image quality metric described in the following section (**Supporting Information Figure S1**)

Network Training

We train the model in a combination of L_p loss and gradient difference loss (38) between the prediction $\hat{\mathbf{x}}$ and ground truth \mathbf{x} :

$$\mathcal{L}(\hat{\mathbf{x}}, \mathbf{x}) = \mathcal{L}_p + \lambda \mathcal{L}_{gdl} \quad [6]$$

where $\mathcal{L}_p(\hat{\mathbf{x}}, \mathbf{x}) = \|\hat{\mathbf{x}} - \mathbf{x}\|_p^p$ and $\mathcal{L}_{gdl}(\hat{\mathbf{x}}, \mathbf{x}) = \left| |\nabla_x \hat{\mathbf{x}}| - |\nabla_x \mathbf{x}| \right| + \left| |\nabla_y \hat{\mathbf{x}}| - |\nabla_y \mathbf{x}| \right|$. We choose to use $p=1$ (i.e., L1 loss) instead of $p = 2$ (L2 loss) because L1 loss is known to provide a sharp image prediction. We also add the gradient difference loss because directly penalizing the differences of image gradient also enhances the sharpness of the image prediction (38). We set $\lambda = 1$. We report the experimental results on the performance of choosing the different values of λ and choosing between L1 and L2 in **Supporting Information Figure S2**.

For optimizing the network parameters, we use ADAM optimizer (39) with a learning rate of 0.001, a mini-batch size of 64, and 200 epochs. We implement the network

with Keras using Tensorflow backend. The network is trained using a 16-core Intel Xeon E5-2698 v3 CPU and a graphical processing unit of Nvidia Tesla K80.

Generation of Training Data

We acquired data from 33 subjects on a 1.5T scanner (Signa Excite, GE Healthcare, Waukesha, WI) at our institution using a standard vocal-tract protocol (6). The imaging protocol was approved by our Institutional Review Board. A 13-interleaf spiral-out spoiled gradient echo pulse sequence was used with the body coil for RF transmission and a custom 8-channel upper airway coil for signal reception. Imaging was performed in the mid-sagittal plane while subjects being scanned followed a wide variety of speech tasks to capture various articulatory postures. Imaging parameters used included: TR = 6.004 ms, TE = 0.8 ms, $T_{read} = 2.52$ ms, spatial resolution = 2.4×2.4 mm², slice thickness = 6 mm, FOV = 200×200 mm², receiver bandwidth = ± 125 kHz, and flip angle = 15°.

Although this protocol uses a short spiral readout (2.52 ms), we found the off-resonance in this data corpus to be diverse and necessary to be corrected to obtain high-quality images. We applied a recently proposed method (**DORC**)(15) to estimate dynamic field maps and to reconstruct dynamic images in conjunction with off-resonance correction. The resultant dynamic images (and field maps) were of size $84 \times 84 \times 400$ (time) for each subject. We regarded these images (\mathbf{x}) and estimated field maps (\mathbf{f}) as ground truth. We split 33 subjects into 23, 5, and 5 subjects for the training, validation, and test sets, respectively. The validation set was used for choosing network parameters and performing validation experiments. The test set was used for evaluating the performance of the proposed method.

Blurred images $\tilde{\mathbf{x}}$ were simulated from the ground truth \mathbf{x} with augmented field maps \mathbf{f}' by employing Equation [2] $\tilde{\mathbf{x}} = \mathbf{A}_0^T \mathbf{W} \mathbf{A}_f \mathbf{x}$ frame by frame as illustrated in **Figure 2 (A)**. Augmentation included a scale α and an offset β to the field map \mathbf{f} such that $\mathbf{f}' = \alpha \mathbf{f} + \beta$ and synthesizing blurred images was based on the augmented field map. Note that $\alpha \neq 0$ would inherit original spatially varying off-resonance blur from the field maps \mathbf{f} up to scale, whereas $\alpha = 0$ leads to spatially uniform blur analogous to the work of Zeng et al (29). We added the offset β to simulate the zeroth-order frequency offsets in image space. Such offsets are a typical result of imperfect shimming. We considered four different spiral trajectories (**Supporting Information Figure S3**).

Those correspond to 13-, 8-, 6-, 4-interleaf spiral-out samplings, with readout times (T_{read}) of 2.52, 4.02, 5.32, and 7.94 ms, respectively, with the same field of view and in-plane resolution.

Figure 2B contains examples of the synthetic images. During implementation of A_f in Equation [2], we approximated $e^{-i2\pi f_j(t_i+T_E)}$ as $e^{-i2\pi f_j(t_i+T_E)} = \sum_{l=1}^L b_{il}c_{lj}$ as described in Equations 19 and 20 of Fessler et al. (28) and executed A_f with $L=6$ times non-uniform FFT (**NUFFT**) (40) calls.

Validation Experiments

Here, we evaluated the impact of various data augmentation strategies (for f) on deblurring performance and generalization. Specifically, we trained the same network architecture using reference data from 23 subjects synthesized with different combinations of the scale factor α , frequency offset β , readout duration T_{read} (spiral trajectories), and the training data size as summarized in **Table 1**. We then measured the effectiveness of the different configurations by using the validation set (5 subjects) listed in **Table 1**.

EXP I-A. Off-resonance range: The off-resonance frequency range is typically unknown. We examined the impact of off-resonance frequency range (f_{max} denoting the maximum frequency value) in training data on deblurring performance. We trained the network on training data simulated with the 4 different values of f_{max} using $\alpha \in \{\frac{1}{6}, \frac{1}{3}, \frac{2}{3}, 1\}$, resulting in four trained networks, and compared their model performance on validation data with varying f_{max} as listed in **Table 1**. We considered $\beta = 0$ and $T_{\text{read}} = 2.52$ ms for both training and validation sets. Note that the frequency range from -625 to 625 Hz ($f_{\text{max}} = 625$ Hz) for the original field maps (i.e., when $\alpha = 1$ and $\beta = 0$).

EXP I-B. Frequency offset and training set size: We added a frequency offset β when synthesizing the training data. This is equivalent to simulating a constant frequency offset over image space. We considered two training configurations; one with $\beta = 0$ and one with $\beta \in \{-300, -200, \dots, 300\}$. The former had N ($= 9200$) samples, while the latter had different sample sizes from N to $7N$. The range of β from -300 to 300 Hz is deliberately chosen broad to cover the maximum center frequency error that could be expected.

EXP II. Spatially varying versus spatially uniform blur: Recent work by Zeng et al. (29) generated training data by simulating off-resonance at evenly spaced frequencies

between ± 500 Hz. This approach, if generalized to spatially varying blur, could benefit situations where the field map is not available for synthesizing spatially varying blur. To test the generalizability of this approach and more importantly the necessity of the field maps for spatially variant blur, we generated synthetic data of spatially invariant blur by setting $\alpha = 0$ and $\beta \in \{-600, -550, \dots, 600\}$ and of spatially variant blur by using $\alpha = 1$ and $\beta \in \{-300, -200, \dots, 300\}$, the same setting as in EXP I-B. We then tested each trained network to another configuration setting by considering two validation configurations of spatially variant and invariant blur listed in **Table 1**.

EXP III. Readout duration: We investigated whether a network trained on a particular T_{read} (spiral trajectory) can be generalized to unseen T_{read} in test time. We used 13-, 8-, 6-, 4-arms trajectories corresponding to T_{read} of 2.52, 4.02, 5.32, 7.94 ms to synthesize blur data, while setting $\alpha = 1$ and $\beta \in \{-300, -200, \dots, 300\}$.

For all experiments, the accuracy and robustness of deblurring performance were evaluated using multiple image quality metrics. We used the high frequency normalized error norm (**HFEN**) (41), due to the expectation that high spatial frequency features would be restored after the blurred boundary is recovered. We also used common metrics, such as peak-signal-to-noise ratio (**PSNR**) and structural similarity index (**SSIM**) (42).

Evaluation using Synthetic Test Data

We tested the model on unseen synthetic test data from 5 subjects (independent from training and validation datasets). We used the model trained in *EXP III*. The test data were simulated from all spiral trajectories without any augmentation (i.e., $\alpha = 1$, $\beta = 0$). For comparison, we applied 1) frequency-segmentation-based multi-frequency interpolation (**MFI**) (22) and 2) model-based iterative reconstruction (**IR**) (27) into the synthetically generated test k-space data (\mathbf{y}). For MFI, we obtained a deblurred image by $\hat{\mathbf{x}} = \mathbf{A}_f^T \mathbf{W} \mathbf{y}$. For IR, we obtained a deblurred image by solving $\min_x \|\mathbf{y} - \mathbf{A}_f \mathbf{x}\|_2^2$ iteratively by using conjugate gradient with 16 iterations. In both methods, we used the ground truth field map \mathbf{f} to construct \mathbf{A}_f . HFEN, PSNR, and SSIM metrics were used for evaluation.

It is worth noting that IR method is known to provide more accurate result than non-IR method for abruptly varying off-resonance in space. This IR approach could

provide the best achievable deblurring performance given the ground truth field map f , although it is not available in practice.

Evaluation using Real Experimental Data

We applied the trained network to real data. We acquired spiral RT-MRI data with four readout durations (2.52, 4.02, 5.32, 7.94 ms) from two subjects and performed image reconstruction as described by Lingala et al (6). We performed the deblurring on the reconstructed images frame by frame by using the trained network. We compared results with DORC (15). This auto-calibrated method estimates dynamic field maps from single-TE blurred image itself after coil phase compensation, with no scan time penalty and iteratively reconstructs off-resonance-corrected image using the estimated field map.

RESULTS

Figure 1B visualizes the representative examples of learned 9×9 kernels of the first convolutional layer. Kernels shown at the left and right were applied to real and imaginary input channels, respectively. Some of kernels are shown to be circular symmetric with varying degree of sharpness, which is similar to off-resonance-induced PSFs observed in spiral trajectories.

Validation Experiments

Figure 3A shows deblurring performance (SSIM and PSNR) as a function of the range of off-resonance (f_{\max}) in the train and validation sets (EXP I-A). For corrected images, each curve represents a separate network trained with different f_{\max} . For no correction (a, black dashed curve), the values of SSIM and PSNR gradually decrease as f_{\max} increases in the validation sets, which is likely due to worsened blurring artifact. All but the network trained with f_{\max} of 104 Hz (b, blue curve) improve image quality for all f_{\max} tested compared with the uncorrected case. Each network is shown to exhibit the highest values of SSIM and PSNR for validation data f_{\max} , with which the network is trained. Performance then quickly degrades for f_{\max} greater than that of its best performance (see c, orange curve). In **Figure 3B**, representative frames are shown. Uncorrected image presents $f_{\max} = 625$ Hz as shown in (a) and model trained with f_{\max} of 625 Hz shown in (e) exhibits the best deblurring performance qualitatively against other models shown in (b-

d). We observe that it is essential for the frequency range of the training set to be a superset of the validation data.

We also found that adding frequency offsets when synthesizing the training data help the network perform better, which is shown in **Table 2** (EXP I-B). In addition, as the training samples increase from N to $7N$, the performance improvement can be found of 2.1, 0.003, and 0.022 in PSNR, SSIM, and HFEN, respectively.

Table 3 presents the average PSNR, SSIM, and HFEN values for the quantitative comparison of model performance on spatially invariant and variant blur (EXP II). The network trained on spatially variant blur has superior PSNR, SSIM, and HFEN values for both validation data of spatially invariant and variant when compared to no correction and the network trained on spatially invariant blur. The network trained on spatially invariant blur improves all the image metrics for the validation data of spatially invariant blur compared to no correction, but when applied to spatially variant blur, presents even lower values in all the metrics than no correction, indicating it fails to deblur spatially varying off-resonance.

Figure 4 presents image metrics as a function of readout duration (T_{read}) in the train and validation sets (EXP III). Regardless of T_{read} used for training networks, PSNR, SSIM, and HFEN are improved after correction when compared to no correction. For each of T_{read} tested, the network trained with the corresponding T_{read} has superior PSNR, SSIM, and HFEN compared to networks trained with other T_{read} (see arrows). For each trained network, the best performance is almost always achieved when both T_{read} in the training and validation sets are the same and then performance quickly degrades for longer T_{read} than that with which each was trained. It can be found that there is no single network that is trained for a particular T_{read} but works best for all other T_{read} tested, whereas the network trained using all the T_{read} as indicated by “All included” (green) in Figure 4 exhibits improvement comparable to individually trained networks.

Evaluation using Synthetic Data

Figure 5 compares image metric results as a function of T_{read} for images with no correction and after correction using various methods applied to synthetic test data of 5 subjects. The proposed method (purple) is compared against no correction (blue), MFI (red), and IR (orange). For all methods, performance gradually degrades as readout

duration increases. Overall, IR has superior PSNR, SSIM, and HFEN values for all readout durations, followed by the proposed method, MFI, and no correction. MFI had lower PSNR than that for no correction for readout duration longer than 2.52 ms (black arrows), which is likely due to the air-tissue boundary presenting abrupt spatially varying off-resonance that would violate its inherent assumption for longer spiral readouts.

Figure 6 contains representative image frames of the ground truth, uncorrected image, and images corrected by various comparison methods. In Figure 6A, blurring is clearly seen around the lips, tongue surface, and soft palate in the uncorrected image (yellow arrows). After correction, MFI even deteriorates the delineation of the boundaries in those regions, whereas the IR method almost perfectly resolves the blurring artifact as also clearly observed in the difference images (Figure 6B). The proposed method successfully resolves the blurring artifact in those regions, which is visually comparable to the result from IR. Figure 6C shows the intensity time profiles that are extracted at the dotted line marked in the ground truth. Both IR and the proposed methods exhibit sharp boundary between tongue and air and around soft palate, which is consistent over time frames.

Evaluation using Real Experimental Data

Figure 7 contains representative experimental data using different spiral readout durations. Image is reconstructed with no off-resonance correction and using the state-of-the-art method. The proposed method took the uncorrected images (left column) as an input to the trained network and performed deblurring frame-by-frame. In the uncorrected image, off-resonance blurring is most clearly observed at the lower lip (green arrows) and hard palate (red arrows) and becomes severe with the longer readouts. The proposed method is able to improve delineation of boundaries in those locations. For example, the lower lip becomes sharper and the structure of the hard plate becomes visible after correction using the proposed method (see red arrows), which is consistent for all readout durations considered. The previous method exhibits improved depiction of air-tissue boundaries for short readouts (≤ 5.32 ms) but signal intensity in several regions becomes spuriously amplified, and the blurred anatomic structures remain still unresolved for longer spiral readouts (7.94 ms) (see yellow arrows).

DISCUSSION and CONCLUSION

We have demonstrated a machine learning method for correcting off-resonance artifacts in 2D spiral RT-MRI of human speech production without exam-specific field maps. We utilized a simple 3-layer CNN to learn an end-to-end mapping between distorted and distortion-corrected images. We trained the CNN model using spatially varying off-resonance blur synthetically generated by using the discrete object approximation and field maps. Once the network is trained, the proposed method is computationally fast (12.3 ± 2.2 ms per-frame on a single GPU) and effective at resolving spatially varying blur that occurs most significantly at the vocal tract air-tissue boundaries of interest. Performance was superior to a current state-of-the-art auto-calibrated method and only slightly inferior to ideal reconstruction with perfect knowledge of the field map.

To train the proposed network architecture, we synthetically generated spatially varying off-resonance blur using reference data with field maps estimated from the auto-calibrated method with affine linear data augmentation of the field maps ($f' = \alpha f + \beta$). This is different from the approach taken by Zeng et al. (29) where spatially invariant off-resonance was simulated at a range of off-resonance frequencies. We experimentally found that our network architecture trained for spatially invariant blur would not be able to resolve spatially varying blur, and the usage of spatially-varying field maps is valuable (EXP II). This is consistent with one of the critical assumptions underlying machine learning that unseen test data comes from the same distribution as training data. We also investigated generalizability with respect to readout duration. We found that readout duration of the training and test sets should be same in order for the network to correct off-resonance without performance degradation (EXP III). This is consistent with expectation, because each readout (trajectory) presents a unique PSF for a given off-resonance frequency, which might not be generalized by other readout unless data from other readouts are also present during the training phase. One exception would be spiral imaging with extremely short echo time.

We compared the proposed method with several conventional methods. For the synthetic test data, MFI exhibited the worst performance (Figure 5), which is likely due to the air-tissue boundary presenting abrupt spatially varying off-resonance. Model-based IR with knowledge of the true field map was superior to all others in terms of PSNR,

SSIM, and HFEN. While being impractical, poor measurements or estimates of the field map for MFI and IR methods or any conventional method can severely degrade image quality. One such case is shown in Figure 7, where auto-calibrated methods do not reliably work at longer readout durations (7.94 ms). This is because the field maps are estimated from the severely distorted images and this error propagates to the estimated field maps and to the iterative off-resonance correction procedure. The proposed method avoids this issue and provides superior performance even at longer spiral readout than the iterative approach.

We used a simple 3-layer CNN architecture, which is motivated by analogy to traditional deblurring procedures. With the continually growing number of state-of-the-art network architectures, many of which are much deeper, we expect that there is further room for improvement. Nevertheless, there should be a balance between performance and the ability to explain such performance. The purpose of this study was to demonstrate feasibility of spatially varying off-resonance correction using a simple CNN architecture, and this was achieved. We only examined a single contrast and a single region of body. A larger study encompassing multiple body regions with different imaging parameters would be valuable in future work.

We considered speech production application because off-resonance artifacts significantly hamper the detailed speech scientific and linguistic analyses using the dynamic imaging data. The proposed method has shown to provide sharp delineation of articulator boundary with readouts up to ~ 8 ms at 1.5 T, which is 3-fold longer than the current standard practice (16) and would provide 1.7-fold improvement in scan efficiency. This would allow for improved accuracy and precision of speech analysis beginning with boundary segmentation (43–45) that is often impaired by blurring artifact (15). It would also potentially be feasible to achieve higher temporal resolution using longer readout with image quality comparable to short readout (Figure 7) or to use spiral readouts at higher field strengths such as 3 T where SNR is higher and which is available on more sites. The low-latency processing of off-resonance deblurring (12.3 ± 2.2 ms per-frame) without field map would also be valuable for other RT-MRI applications such as cardiac studies and interventional RT-MRI where off-resonance at the lateral wall, adjacent to draining veins, or around metal implants and tools impedes diagnostic use of RT-MRI.

ACKNOWLEDGEMENTS

This work was supported by NIH Grant R01DC007124 and NSF Grant 1514544. We acknowledge the support and collaboration of the Speech Production and Articulation kNowledge (SPAN) group at the University of Southern California, Los Angeles, CA, USA. We also thank Yannick Bliesener for invaluable discussion and constructive feedback on this work.

REFERENCES

1. Ahn CB, Kim JH, Cho ZH. High-speed spiral-scan echo planar NMR imaging-I. *IEEE Trans Med Imaging*. 1986;5:2-7.
2. Meyer CH, Hu BS, Nishimura DG, Macovski A. Fast spiral coronary artery imaging. *Magn Reson Med*. 1992;28:202-13.
3. Nishimura DG, Irarrazabal P, Meyer CH. A velocity k-space analysis of flow effects in echo-planar and spiral imaging. *Magn Reson Med*. 1995;33:549-56.
4. Gatehouse PD, Firmin DN. Flow distortion and signal loss in spiral imaging. *Magn Reson Med*. 1999;41:1023-31.
5. Kim YC, Narayanan SS, Nayak KS. Flexible retrospective selection of temporal resolution in real-time speech MRI using a golden-ratio spiral view order. *Magn Reson Med*. 2011;65:1365-1371.
6. Lingala SG, Zhu Y, Kim Y, Toutios A, Narayanan SS, Nayak KS. A fast and flexible MRI system for the study of dynamic vocal tract shaping. *Magn Reson Med*. 2017;77:112-125.
7. Kerr AB, Pauly JM, Hu BS, Li KC, Hardy CJ, Meyer CH, Macovski A, Nishimura DG. Real-time interactive MRI on a conventional scanner. *Magn Reson Med*. 1997;38:355-367.
8. Yang PC, Kerr AB, Liu AC, Liang DH, Hardy C, Meyer CH, Macovski A, Pauly JM, Hu BS. New real-time interactive cardiac magnetic resonance imaging system complements echocardiography. *J Am Coll Cardiol*. 1998;32:2049-56.
9. Nayak KS, Pauly JM, Kerr AB, Hu BS, Nishimura DG. Real-time color flow MRI. *Magn Reson Med*. 2000;43:251-8.
10. Nayak KS, Cunningham CH, Santos JM, Pauly JM. Real-time cardiac MRI at 3 tesla. *Magn Reson Med*. 2004;51:655-660.

11. Narayanan SS, Nayak KS, Lee S, Sethy A, Byrd D. An approach to real-time magnetic resonance imaging for speech production. *J Acoust Soc Am*. 2004;115:1771–1776.
12. Steeden JA, Kowalik GT, Tann O, Hughes M, Mortensen KH, Muthurangu V. Real-time assessment of right and left ventricular volumes and function in children using high spatiotemporal resolution spiral bSSFP with compressed sensing. *J Cardiovasc Magn Reson*. 2018;20:1–11.
13. Block KT, Frahm J. Spiral imaging: a critical appraisal. *J Magn Reson Imag*. 2005;21:657–668.
14. Sutton BP, Conway CA, Bae Y, Seethamraju R, Kuehn DP. Faster dynamic imaging of speech with field inhomogeneity corrected spiral fast low angle shot (FLASH) at 3 T. *J Magn Reson Imag*. 2010;32:1228–1237.
15. Lim Y, Lingala SG, Narayanan SS, Nayak KS. Dynamic off-resonance correction for spiral real-time MRI of speech. *Magn Reson Med*. 2019;81:234–246.
16. Lingala SG, Sutton BP, Miquel ME, Nayak KS. Recommendations for real-time speech MRI. *J Magn Reson Imag*. 2016;43:28–44.
17. Reeder SB, Hu HH, Sirlin CB, Group LI, Diego S. Non-Cartesian balanced SSFP pulse sequences for real-time cardiac MRI. *Magn Reson Med*. 2016;75:1546–1555.
18. Liu H, Martin AJ, Truwit CL. Interventional MRI at high-field (1.5 T): needle artifacts. *J Magn Reson Imag*. 1998;8:214–9.
19. Shenberg I, Macovski A. Inhomogeneity and multiple dimension considerations in magnetic resonance imaging with time-varying gradients. *IEEE Trans Med Imaging*. 1985;4:165–74.
20. Maeda A, Sano K, Yokoyama T. Reconstruction by weighted correlation for MRI with time-varying gradients. *IEEE Trans Med Imaging*. 1988;7:26–31.
21. Noll DC, Meyer CH, Pauly JM, Nishimura DG, Macovski A. A homogeneity correction method for magnetic resonance imaging with time-varying gradients. *IEEE Trans Med Imaging*. 1991;10:629–637.
22. Man LC, Pauly JM, Macovski A. Multifrequency interpolation for fast off-resonance correction. *Magn Reson Med*. 1997;37:785–792.
23. Nayak KS, Tsai CM, Meyer CH, Nishimura DG. Efficient off-resonance correction for spiral imaging. *Magn Reson Med*. 2001;45:521–524.

24. Chen W, Meyer CH. Semiautomatic off-resonance correction in spiral imaging. *Magn Reson Med.* 2008;59:1212–1219.
25. Makhijani MK, Nayak KS. Exact correction of sharply varying off-resonance effects in spiral MRI. *Proc IEEE Int Symp Biomed Imaging.* Arlington, VA, 2006, pp. 730–733.
26. Noll DC. Reconstruction techniques for magnetic resonance imaging. Ph.D. thesis, Stanford University. 1991.
27. Sutton BP, Noll DC, Fessler JA. Fast, iterative image reconstruction for MRI in the presence of field inhomogeneities. *IEEE Trans Med Imaging.* 2003;22:178–188.
28. Fessler JA, Member S, Lee S, Member S, Olafsson VT, Shi HR, Noll DC. Toeplitz-based iterative image reconstruction for MRI with correction for magnetic field inhomogeneity. *IEEE Trans Signal Proc.* 2005;53:3393–3402.
29. Zeng DY, Shaikh J, Holmes S, Brunsing RL, Pauly JM, Nishimura DG, Vasanaawala SS, Cheng JY. Deep residual network for off-resonance artifact correction with application to pediatric body MRA with 3D cones. *Magn Reson Med.* 2019;82:1398–1411.
30. Noll DC, Pauly JM, Meyer CH, Nishimura DG, Macovski A. Deblurring for non-2D Fourier transform magnetic resonance imaging. *Magn Reson Med.* 1992;25:319–333.
31. Man LC, Pauly JM, Macovski A. Improved automatic off-resonance correction without a field map in spiral imaging. *Magn Reson Med.* 1997;37:906–913.
32. Lim Y, Lingala SG, Narayanan S, Nayak KS, Angeles L. Improved depiction of tissue boundaries in vocal tract real-time MRI using automatic off-resonance correction. *Proc INTERSPEECH*, San Francisco, CA, USA, 2016. pp. 1765–1769
33. Ye JC, Sung WK. Understanding geometry of encoder-decoder CNNs. arXiv:1901.07647; 2019.
34. Bresch E, Kim YC, Nayak KS, Byrd D, Narayanan SS. Seeing speech: Capturing vocal tract shaping using real-time magnetic resonance imaging. *IEEE Signal Process Mag.* 2008;25:123–129.
35. Scott AD, Wylezinska M, Birch MJ, Miquel ME. Speech MRI: morphology and function. *Phys Med.* 2014;30:604–618.
36. Denis L, Thiébaud E, Soulez F, Becker JM, Mourya R. Fast approximations of shift-variant blur. *Int J Comput Vis.* 2015;115:253–278.
37. Schenck JF. The role of magnetic susceptibility in magnetic resonance imaging: MRI magnetic compatibility of the first and second kinds. *Med Phys.* 1996;23:815–50.

38. Mathieu M, Couprie C, LeCun Y. Deep multi-scale video prediction beyond mean square error. arXiv:1511.05440; 2016.
39. Kingma DP, Ba J. Adam: a method for stochastic optimization. arXiv:1412.6980; 2014.
40. Fessler JA, Sutton BP. Nonuniform fast Fourier transforms using min-max interpolation. *IEEE Trans Signal Proc.* 2003;51:560–574.
41. Ravishankar S, Bresler Y. MR image reconstruction from highly undersampled k-space data by dictionary learning. *IEEE Trans Med Imaging.* 2011;30:1028–1041.
42. Wang Z, Bovik AC, Sheikh HR, Simoncelli EP. Image quality assessment: from error visibility to structural similarity. *IEEE Trans Image Process.* 2004;13:600–612.
43. Bresch E, Narayanan SS. Region segmentation in the frequency domain applied to upper airway real-time magnetic resonance images. *IEEE Trans Med Imaging.* 2009;28:323–338.
44. Kim J, Kumar N, Lee S, Narayanan SS. Enhanced airway-tissue boundary segmentation for real-time magnetic resonance imaging data. *Proc Int Seminar on Speech Production (ISSP)*, Cologne, Germany, 2014. pp. 222–225.
45. Somandepalli K, Toutios A, Narayanan SS. Semantic edge detection for tracking vocal tract air-tissue boundaries in real-time magnetic resonance images. *Proc INTERSPEECH*, Stockholm, Sweden, 2017. pp. 631–635.

FIGURES

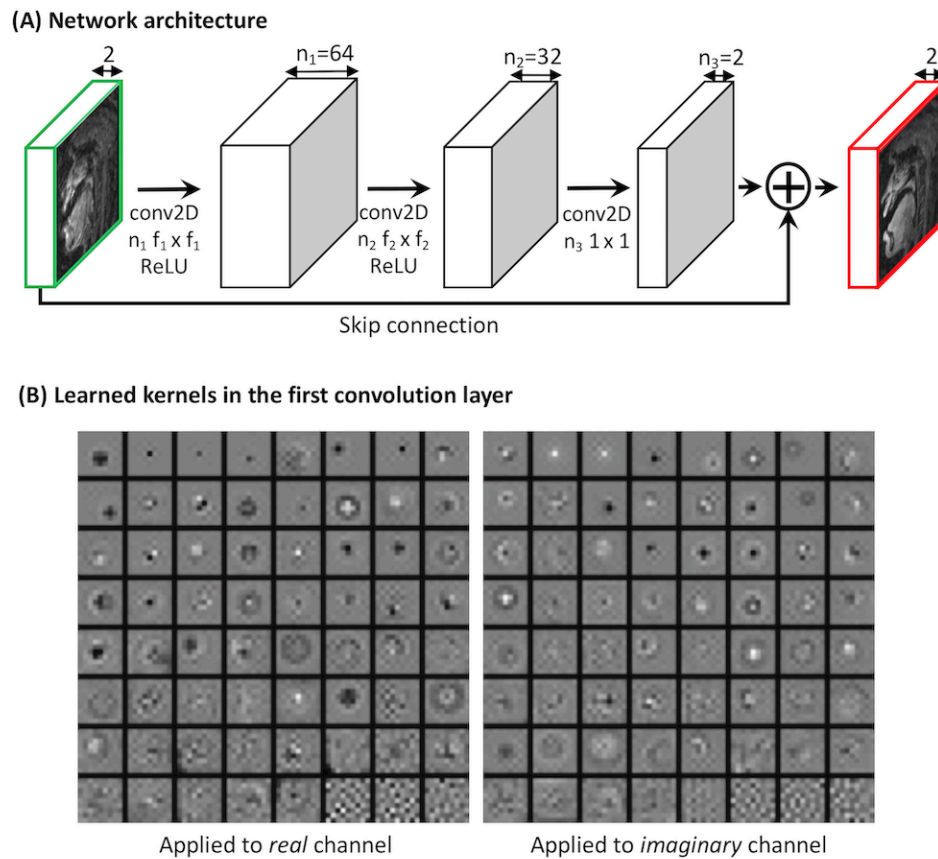


Figure 1. Proposed Network. (A) Network architecture. The input is distorted complex images, and the output is distortion-free complex images, each consisting of two channels (real and imaginary). The network is composed of 3 convolutional layers. The first two layers apply 2D convolution, followed by ReLU while the last layer applies 1×1 convolution. The input to the first layer is added to the output of the last layer via skip connection. (B) Representative examples of learned 9×9 convolution kernels ($f_1=9$). The 128 learned kernels are applied to real (64 at left) and imaginary (64 at right) input channels in the first layer. The majority of kernels exhibit circular symmetry which corresponds to the expected shape of off-resonance PSFs in spiral MRI.

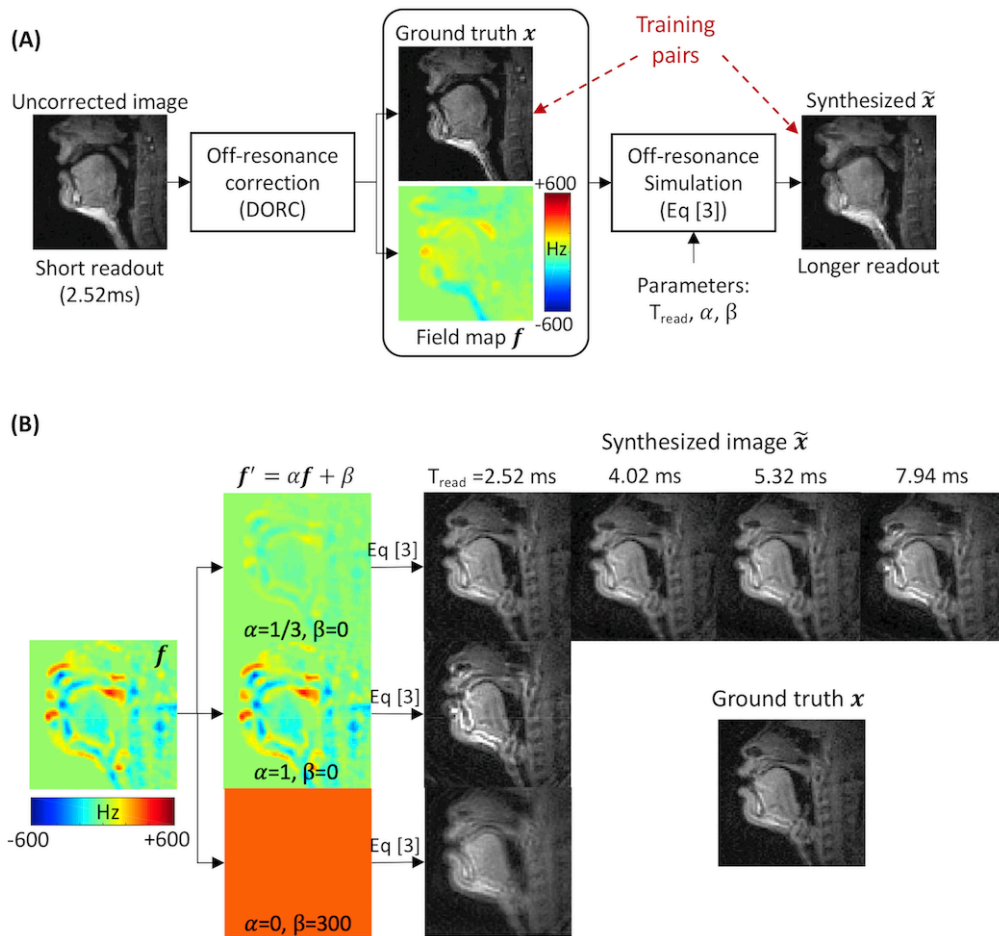


Figure 2. Generation of training data. (A) The ground truth image x and field map f are obtained from short readout (2.52 ms) data with off-resonance estimation and correction (15). Blurred images \tilde{x} are synthesized via simulating (Eq. [3]) using the ground truth image x and field map f' augmented by α and β and different spiral readout durations (T_{read}). (B) The field maps are augmented by scaling and constant offset $f' = \alpha f + \beta$ with α ranging from 0 to 1 and β from -300 to 300 Hz. We also consider four different spiral readout durations ($T_{\text{read}} = 2.52, 4.02, 5.32, \text{ and } 7.94$ ms). Those correspond to 13-, 8-, 6-, 4-interleaf spiral-out trajectories, respectively, with the same field of view and in-plane resolution.

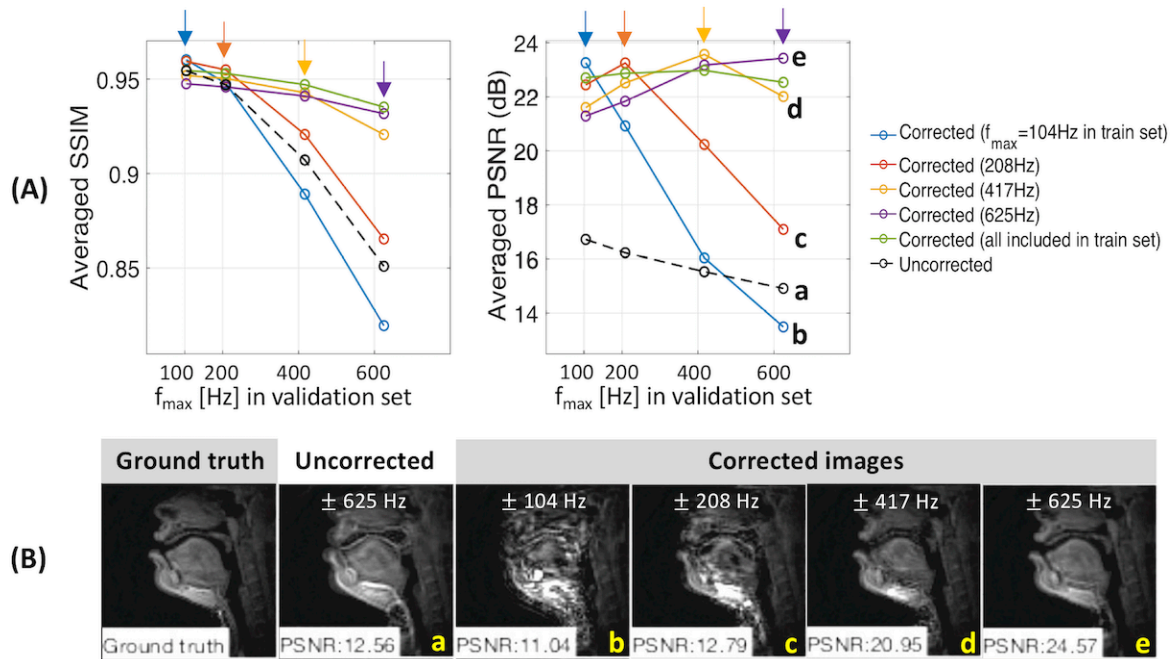


Figure 3. Performance depends on the Training Set (EXP I-A). (A) Averaged SSIM and PSNR as a function of frequency range (f_{\max} denoting the maximum frequency value) for the uncorrected (black dotted) and corrected (non-black solid) images in the validation set. Color (non-black) represents a separate network trained with different f_{\max} . Note that higher SSIM and PSNR correspond to better performance. The best performance is achieved when the training and validation datasets share the same range of off-resonance (arrows). When severe off-resonance appears in the validation data as off-resonance range is increased, performance for the network trained with f_{\max} less than that of the validation data quickly degrades. (B) Representative example of the ground truth, uncorrected, and corrected images. The uncorrected image had $f_{\max} = 625$ Hz, and was deblurred using models trained with f_{\max} of 104, 208, 417, and 625 Hz. We observe that it is essential for the frequency range of the training set to be a superset of the validation set.

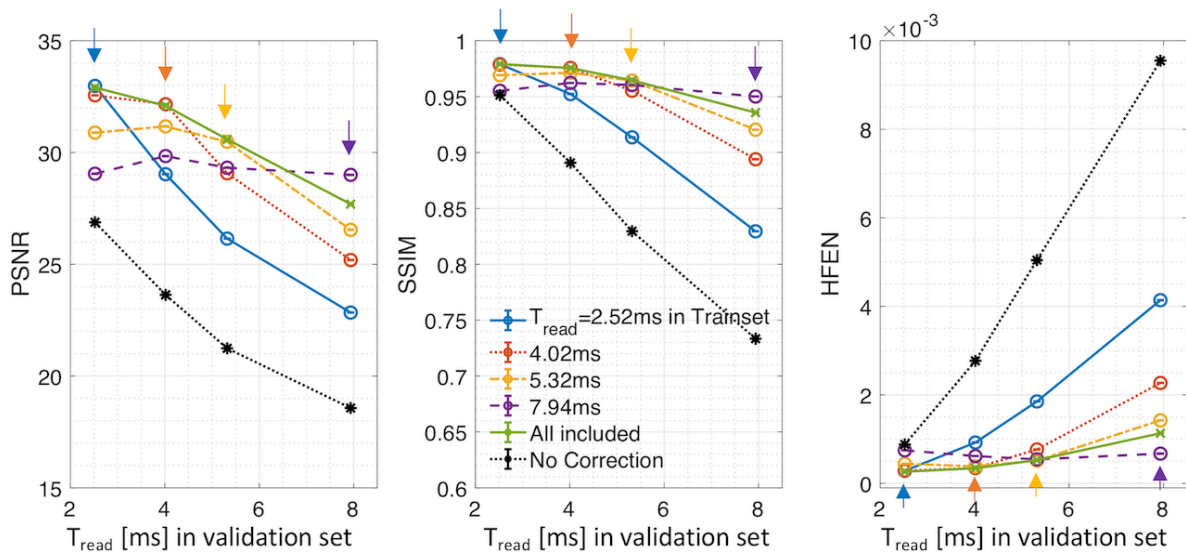


Figure 4. Impact of Readout Duration (EXP III). Image Quality Metrics (PSNR, SSIM, and HFEN) as a function of readout duration (2.52, 4.02, 5.32, and 7.94 ms) for the uncorrected (black) and corrected (non-black) images are shown. For corrected images, color represents a separate network trained with different readout durations; “All included” (green) indicates all of four readout durations are used during training. All metrics are averaged across time and subjects. Note that higher PSNR and SSIM and lower HFEN correspond to better performance. The best performance is almost always achieved when the training and validation datasets share the same readout duration as indicated by arrows in each panel of the image metrics. The performance then quickly degrades for longer readout durations in the validation set than that with which the network was trained.

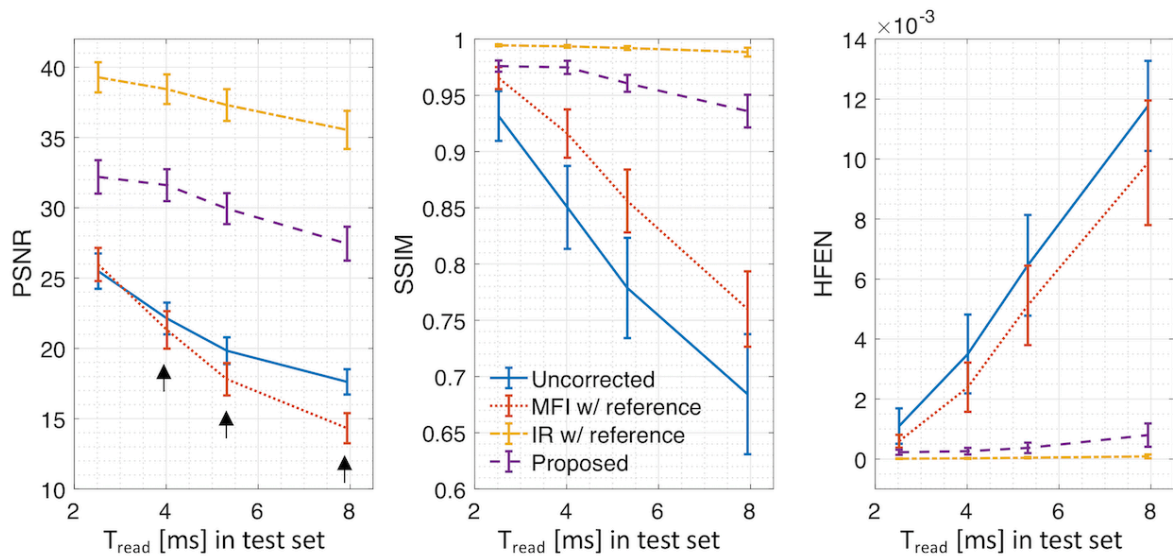


Figure 5. Quantitative comparison of deblurring performance for comparison methods using synthetic test data. Image Quality Metrics (PSNR, SSIM, and HFEN) are shown as a function of readout duration (2.52, 4.02, 5.32, and 7.94 ms). All metrics are averaged across time and subjects and error bars were calculated as the standard deviation. Note that higher PSNR and SSIM and lower HFEN correspond to better performance. The proposed method (purple) is compared against no correction (blue), multi-frequency interpolation (22) (MFI, red), and iterative reconstruction (27) (IR, orange). For all methods, performance gradually degrades as readout duration increases. IR performs best for all readout durations, followed by the proposed method, MFI, and no correction. Note that MFI had lower PSNR than that for no correction for readout duration > 2.52 ms (black arrows).

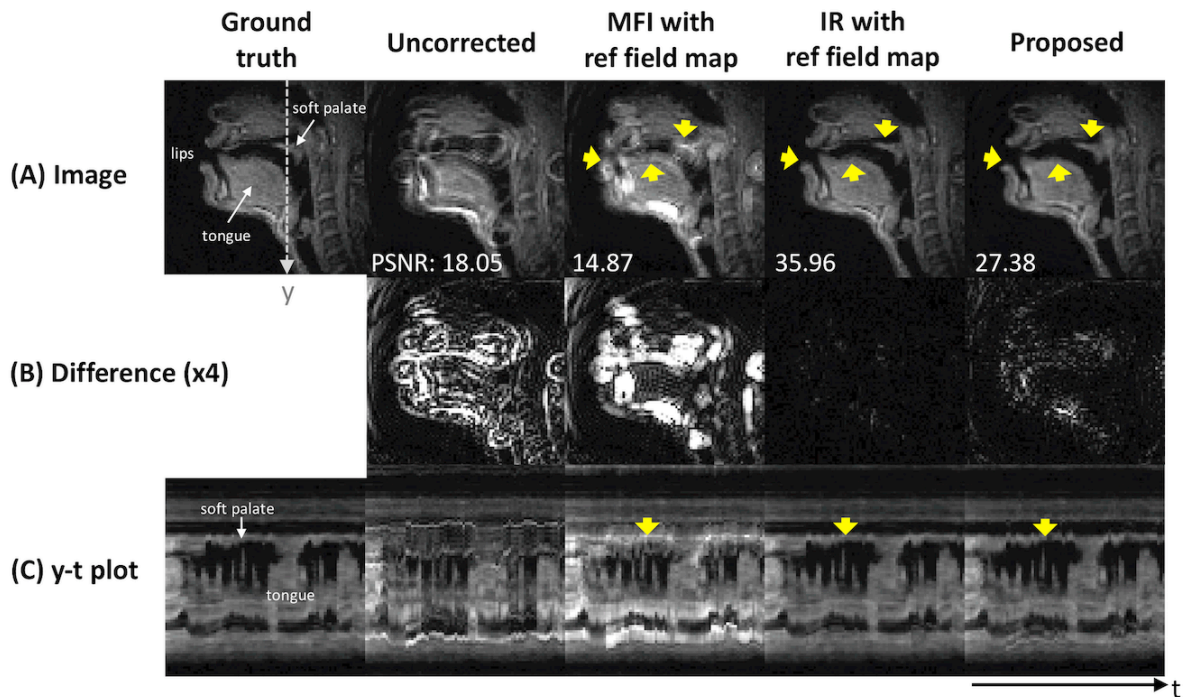


Figure 6. Qualitative comparison of deblurred images for comparison methods using synthetic test data. Left to right: the ground truth, uncorrected, multi-frequency interpolation (MFI) (22), model-based iterative reconstruction (IR) (27), and the proposed method. (A) images before and after deblurring with various methods, (B) absolute difference images (amplified by a factor of 4 for better visualization) with respect to the ground truth, and (C) an intensity vs time (y - t) plot marked by dotted white line in (A). Yellow arrows point out the regions that are most affected by off-resonance blurring and that present contrast in deblurring performance for various methods. The proposed method successfully resolves the blurring artifact, which is superior to uncorrected image and image using MFI, and is visually comparable to IR method that presents the best performance over all others.

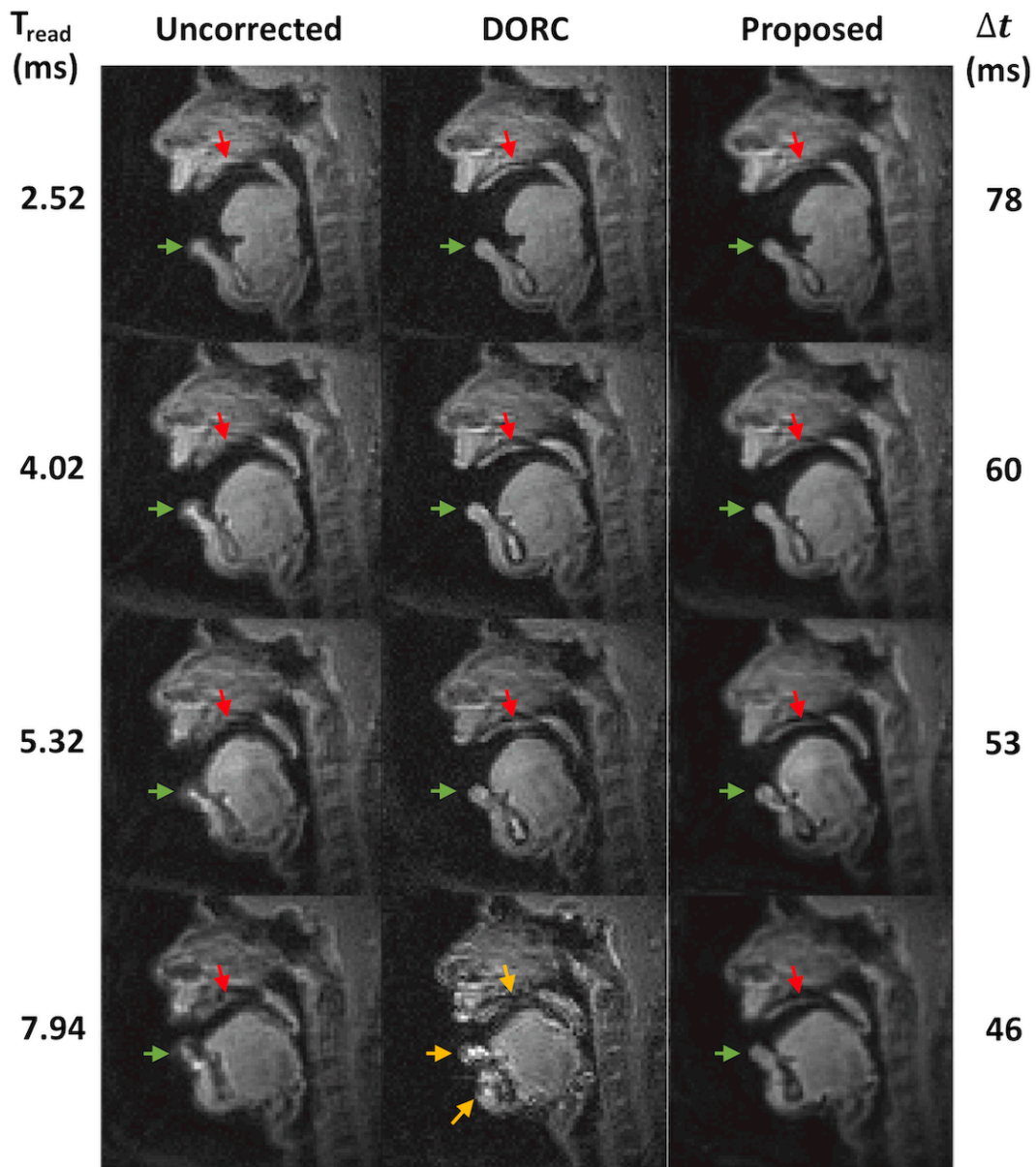


Figure 7. Representative experimental results using long readout spirals. Left to right: Image reconstruction with no off-resonance correction, image reconstruction using a previous auto-calibrated dynamic off-resonance correction (DORC) (15), and image deblurred by the proposed method. Top to bottom: readout duration from 2.52 to 7.94 ms and temporal resolution of 78 (13-interleaf) to 46 ms (4-interleaf). Green (lower lip) and red (hard palate) arrows point out the regions that are most affected by off-resonance blurring and corrected by the DORC and proposed methods. The proposed method provides improved delineation of the boundaries, which is consistent for all readout durations considered, whereas DORC fails to resolve the blurred boundaries for longer

readout duration of 7.94 ms (yellow arrows). See also Supporting Information Videos S1.

TABLES

Table 1. Summary of the parameters used to generate training and validation sets for validation experiments.

		Train				Validation		
		α	β (Hz)	T_{read} (ms)	# of samples	α	β (Hz)	T_{read} (ms)
EXP I	A	1/6 1/3 2/3 1	{0}	2.52	N*	1/6 1/3 2/3 1	{0}	2.52
	B	1	{0} {-300, -200, ..., 300} {-300, -200, ..., 300} {-300, -200, ..., 300}	2.52	N N 3.5N 7N	1	{0}	2.52
EXP II		1 0	{-300, -200, ..., 300} {-600, -550, ..., 600}	2.52	3.5N 4N	1 0	{0} {-300, -200, ..., 300}	2.52
EXP III		1	{-300, -200, ..., 300}	2.52 4.02 5.32 7.94	7N	1	{-300, -200, ..., 300}	2.52 4.02 5.32 7.94

Each row represents a configuration set of α , β , T_{read} , and # of samples for train set or α , β , T_{read} for validation set. *Here, N (# of samples) = 9200 84×84 image pairs of distorted and distortion-free complex images.

Table 2. Quantitative evaluation of model performance in terms of the PSNR, SSIM, and HFEN, without and with offset β , and as a function of the number of training samples (EXP I-B).

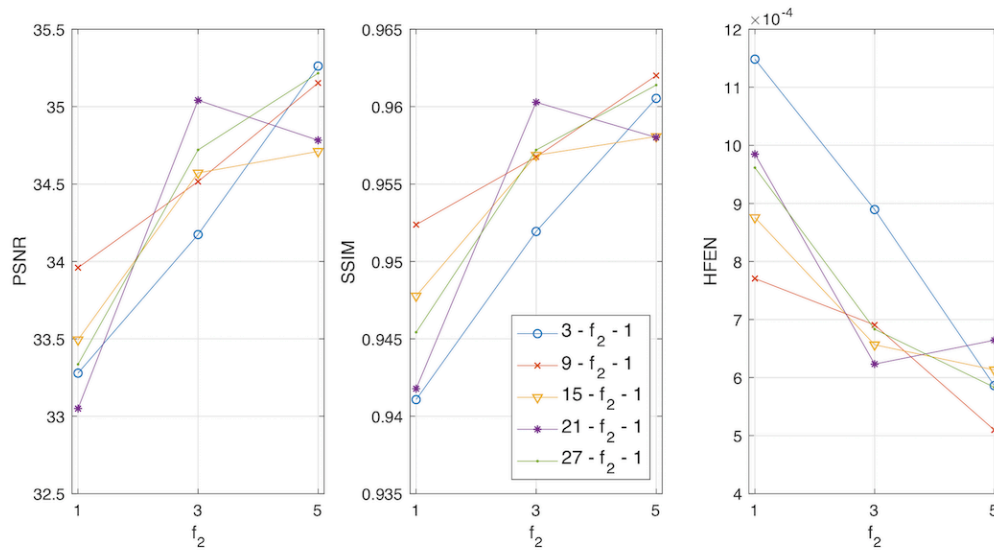
Training data		PSNR	SSIM	HFEN (x1000)
Without offset $\beta (= 0)$	# of samples = N*	32.75	0.979	0.274
	N	33.43	0.980	0.125
With offset β {-300, -200, ..., 300}	3.5N	34.40	0.983	0.094
	7N	34.53	0.983	0.103
No correction		26.82	0.951	0.890

*Here, N = 9200 84×84 image pairs of distorted and distortion-free complex images.

Table 3. Quantitative evaluation of model performance on spatially invariant and variant blur in terms of the PSNR, SSIM, and HFEN (EXP II).

Validation data	Training data	PSNR	SSIM	HFEN (x1000)
Spatially variant blur ($\alpha = 1$ and $\beta = 0$)	no correction	26.82	0.951	0.890
	Spatially variant blur $\alpha = 1$ $\beta \in \{-300, -200, \dots, 300\}$	34.40	0.983	0.094
	Spatially invariant blur $\alpha = 0$ $\beta \in \{-600, -550, \dots, 600\}$	26.53	0.934	1.414
Spatially invariant blur ($\alpha = 0$ and $\beta \in \{-300, -200, \dots, 300\}$)	no correction	27.01	0.897	0.346
	Spatially variant blur $\alpha = 1$ $\beta \in \{-300, -200, \dots, 300\}$	35.60	0.986	0.037
	Spatially invariant blur $\alpha = 0$ $\beta \in \{-600, -550, \dots, 600\}$	35.54	0.986	0.046

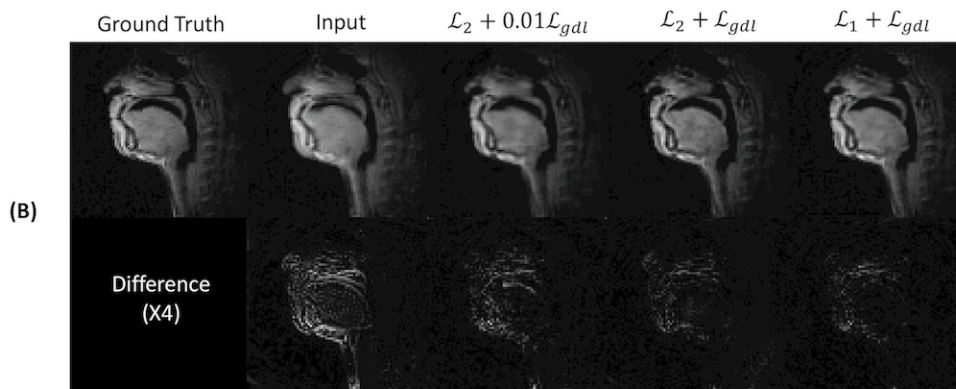
SUPPORTING INFORMATION



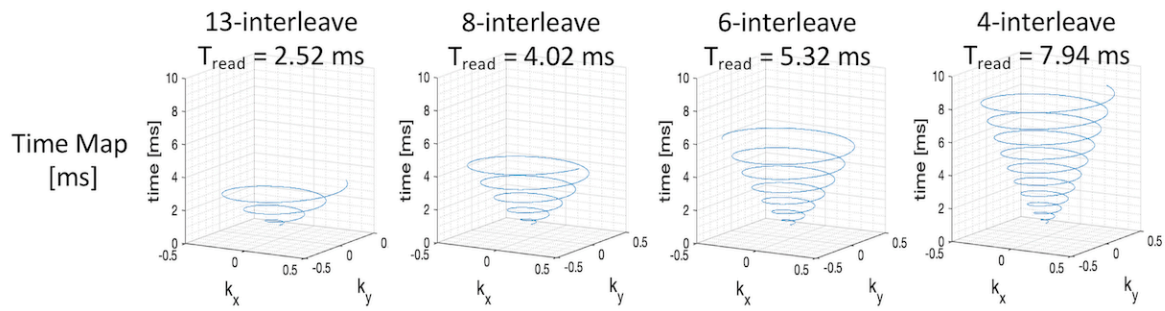
Supporting Information Figure S1. Quantitative comparison of deblurring performance for different filter sizes. Image Quality Metrics (PSNR, SSIM, and HFEN) are shown as a function of filter sizes. Here, the filter size of the first and second convolution layers (f_1 and f_2 , respectively) were varied from 3 to 27 and from 1 to 5, respectively whereas $f_3 = 1$ was kept constant. We choose $f_1 = 9$, $f_2 = 5$, and $f_3 = 1$ ($f_1 - f_2 - f_3 = 9 - 5 - 1$).

(A)

L1 or L2	λ (\mathcal{L}_{gdl})	PSNR	SSIM	HFEN (x1000)
Baseline (input)		27.17	0.851	4.560
L2	$\lambda=0$	33.74	0.949	0.685
	$\lambda=0.01$	33.44	0.946	0.759
	$\lambda=0.1$	33.38	0.946	0.821
	$\lambda=1$	34.68	0.960	0.612
L1	$\lambda=0$	34.96	0.960	0.553
	$\lambda=0.01$	34.69	0.958	0.620
	$\lambda=0.1$	34.85	0.959	0.597
	$\lambda=1$	35.20	0.962	0.589



Supporting Information Figure S2. Combination of L_p loss and gradient difference loss in the model training. (A) Image Quality Metrics (PSNR, SSIM, and HFEN) are shown. L1 loss in a combination with gradient difference loss with $\lambda = 1$ exhibits the highest values of PSNR and SSIM over other combinations. (B) Representative image results for combinations of L_p loss and gradient difference loss. For L2 loss, as gradient difference loss penalty λ increases from 0.01 to 1 (3rd and 4th columns), image sharpness is improved visually. Compared to L2 loss, L1 loss with the same value of λ visually improves the sharpness at the soft palate (4th and 5th columns), although visual difference might not be observed as clearly as that can be observed when increasing λ from 0.01 to 1. We choose to use $p = 1$ and $\lambda = 1$.



Supporting Information Figure S3. Time maps for four different spiral trajectories. Left to right: 13-, 8-, 6-, 4-interleaf spiral-out samplings, with readout times (T_{read}) of 2.52, 4.02, 5.32, and 7.94 ms, respectively, with the same field of view and in-plane resolution. Only one spiral interleave out of fully sampled interleaves is shown here. Here, $TE = 0.8$ ms.

Supporting Information Video S1: Movie display of comparison of representative experimental results using long readout spirals. Left to right: Image reconstruction with no off-resonance correction, image reconstruction using a previous auto-calibrated dynamic off-resonance correction, and image deblurred by the proposed method. Top to bottom: readout duration from 2.52 to 7.94 ms. This supporting information video corresponds to Figure 7.